Preparation and Characterization of Silver−Poly(vinylidene fluoride) Nanocomposites: Formation of Piezoelectric Polymorph of Poly(vinylidene fluoride)

Swarup Manna, Sudip K. Batabyal, and Arun K. Nandi*

Polymer Science Unit, Indian Association for the Cultivation of Science, Jadavpur, Kolkata-700 032, India

Received: March 9, 2006; In Final Form: May 11, 2006

In situ Ag nanoparticles are produced on reduction of Ag^+ with *N,N*-dimethylformamide in the presence of poly(vinylidene fluoride) (PVF_2). The plasmon band transition is monitored with time in the reaction mixture for three sets of experiments by UV−vis spectroscopy. The plasmon band absorbance increases sigmoidally with log(time). Analysis of the data with the Avrami equation yields an exponent *n* value between 1.5 and 2.0, indicating two-dimensional nucleation with linear or diffusion controlled growth. The TEM study of the polymer nanocomposites (PNC) indicates both spherical and rodlike morphology for PNC0.5 and PNC2.5 samples, whereas the PNC11 sample has spherical and agglomerated structures (the numerical number associated with PNC indicates percentage (w/w) of Ag in the nanocomposite). The WAXS and FTIR studies indicate the formation of piezoelectric β-polymorphic PVF_2 in the nanocomposites. The DSC study indicates some increase of the melting point and enthalpy of fusion of PVF_2 in the nanocomposite, although with increase in Ag nanoparticle concentration the increase is smaller. The crystallization temperatures of PNCs also increased, indicating nucleating effect of Ag nanoparticles in the composite. In the TGA curves, the PNCs exhibit a three-step degradation process. The degradation temperatures of PNCs are lower than that of PVF_2. The storage modulus data indicate a significant reinforcement of the mechanical property in the PNCs where also the reinforcement effect decreases with increasing nanoparticle concentration. Both the loss modulus and tan δ plots indicate two peaks; the lower temperature peak has been attributed for glass transition temperature, whereas the higher one has been attributed to a similar type relaxation process for the crystalline−amorphous interface. The increase in the glass transition is marginal for the PNCs, but the increase of later transition temperature is somewhat higher. The FTIR study shows that the dipolar interaction of the $>CF_2$ dipole with the surface charges of Ag nanoparticle stabilizes the nanoparticle in the nanocomposite.

Introduction

Polymer nanocomposites (PNC) have recently drawn great research interest for their unique physical, mechanical, and optical properties. There are two types of polymer nanocomposites: (i) polymer clay nanocomposites[1−6] and (ii) polymer metal or polymer semiconductor nanocomposites.[7−14] In the former case the clay tactoids are dispersed in the nanodimension within the host polymer, whereas in the latter case the metal or semiconductor nanoparticles are dispersed in the host polymer. Both types of nanocomposites exhibit enhancement of physical and mechanical properties of the polymer, but the latter type combines with additional unusual optical, conducting, and chemical properties. In this article, we present the preparation and characterization of the Ag nanoparticle within poly(vinylidene fluoride) (PVF_2) host.

Silver is an important metal to study in the nanodimension due to its very high conductivity in the bulk[15] and also for its attractive optical properties which depend on the nanoparticle shape and size.[16−20] The origin of the special optical properties is due to the interaction of light with the free conducting electrons causing plasmon resonance which is manifested as intense absorption band.[21] The wavelength of the plasmon resonance band depends on particle size, shape, surface charge,

and environment.[22,23] The intense plasmon resonance allows single molecule observation in surface-enhanced Raman scatterings,[24,25] allows coupled Ag particles to form a subwavelength waveguide,[26] and enables sensitive colorimetric DNA screening.[27,28]

PVF_2 is a technologically important polymer that exhibits five different polymorphs in its crystalline state.[29] The most common polymorph is the α-polymorph with monoclinic unit cell and $TGT\bar{G}$ chain conformation.[30,31] This polymorph is piezoelectrically inactive; however, the orthorhombic β-polymorph with all-trans chain conformation is piezoelectrically active.[32,33] The γ-phase also has an orthorhombic unit cell with $T_3GT_3\bar{G}$ chain conformation,[34] but it is piezoelectrically inactive. The δ- and ϵ-polymorphs are polar and antipolar analogues of the α- and γ-forms, respectively.[29,35]

In PVF_2 fluorine is a strongly electronegative element, and the $>CF_2$ dipole may have affinity to the charges present on the nanoparticle surface. In other words, PVF_2 may stabilize nanoparticles through electrostatic interaction. Again PVF_2 is soluble in *N,N*-dimethylformamide (DMF) due to the specific interaction present between the $>CF_2$ dipole of PVF_2 and the carbonyl group[36,37] of DMF. It is also reported that DMF is a reducing agent and can reduce silver ion into metallic silver.[20,38,39] Thus, PVF_2 may stabilize Ag nanoparticles produced in the DMF solution of PVF_2 and $AgNO_3$. In this article we explore this possibility.

Experimental Section

Samples. Poly(vinylidene fluoride) (PVF$_2$) was a product of Solvey Corporation, USA (Sol 1010). The sample was recrystallized from its dilute acetophenone solution, washed with methanol, and finally dried in a vacuum. The mol wt ($\bar{M}_w$) of the sample was measured from GPC using DMF at 90 °C and was found to be 4.48×10^5. The polydispersity value was 2.09, and the H–H defect measured from ^{19}F NMR spectra in *N,N*-DMF-d_7 was 4.19 mol %.

AgNO$_3$ (GR) was purchased from E-Merck India. DMF (GR, E-Merck India) was dried over anhydrous MgSO$_4$ and was then vacuum-distilled. The middle fraction of the distillate was taken for the experiment.

Preparation of Polymer Films with Ag Nanoparticles. The silver (Ag) nanoparticles into the polymer matrix were prepared by mixing 1% (W/V) PVF$_2$ solution in DMF with solid AgNO$_3$ to make the concentration of AgNO$_3$ in the resulting solutions: 2.94×10^{-4} (M) (Set-1), 1.47×10^{-3} (M) (Set-2), and 7.36×10^{-3} (M) (Set-3). These AgNO$_3$ concentrations were chosen to get optimum physical and mechanical properties of the nanocomposites. They were stirred at 30 °C by magnetic stirrer for 13 days. The colorless solutions gradually changed from pale yellow to reddish brown and finally to deep reddish brown for Set-1, violet for Set-2, and gray for Set-3. They were dried on a Petri dish over a hot stage at 60 °C. Finally, they were dried in a vacuum at 60 °C for 3 days. A blank PVF$_2$ film was also prepared by drying the same 1% (w/v) solution in DMF in a way similar to that described above. The samples derived from Set-1, Set-2, and Set-3 were designated as PNC0.5, PNC2.5, and PNC11, where the number indicates percentage (w/w) of Ag in the film.

Characterization. *Microscopy.* A TEM study of the samples was done by dropping one drop of 13-day-old reaction mixture on carbon-coated copper grid, drying it at 60 °C under vacuum, and observing it through a transmission electron microscope (JEOL, model 2010EX) under a voltage of 200 KV.

Spectroscopy. UV–vis spectra of the DMF solutions of PVF$_2$ and Ag nanoparticles (i.e., reaction mixture) were taken at different aging times of the solutions by a Hewlett-Packard UV–vis spectrophotometer (model 8453).

FTIR spectra of the dried films were made using a Nicolet FTIR instrument (Magna-IR750 spectrometer series II).

WAXS Study. Wide-angle X-ray scattering (WAXS) experiments were done for the solvent-cast films using a Seifert X-ray diffractometer (model C3000) with a parallel beam optics attachment. The instrument was operated at a 35 kV voltage and 30 mA current and was calibrated with a standard silicon sample. The samples were scanned from $2\theta = 5°$ at the step scan mode (step size 0.03°, preset time 1 s), and the diffraction pattern was recorded using a scintillation counter detector.

Thermal Study. The thermal properties of the samples were measured using a Perkin-Elmer differential scanning calorimeter (DSC-7) fitted with an intracooler-1. The instrument was operated under N$_2$ atmosphere and was calibrated with Indium before use. The dried samples were put in aluminum pans, and the pans were sealed. They were then heated at the scan rate of 10 °C/min from 30 to 210 °C. The melting temperature and enthalpy of fusion were measured with the help of a computer using a PC series DSC-7 multitasking software (version 3.2).

The thermogravimetric analysis (TGA) of the samples was made using a Mettler Toledo TGA/SDTA 851e instrument under a N$_2$ atmosphere at a heating rate of 10 °C/min from 40 to 700 °C.

Mechanical Property. The mechanical properties of the composite films were measured using a dynamic mechanical analyzer (DMA) (TA Instruments, model Q-800). Films of 25 mm × 5 mm × 0.02 mm dimensions were made from the composites by solution casting on a die, and they were installed on the film tension clamp of the calibrated instrument. The samples were heated from −110 to 150 °C at a heating rate of 10 °C/min. The storage modulus, loss modulus, and tan δ values were measured at a constant frequency of 1 Hz and static force of 0.01 N.

Results and Discussion

Optical Characterization. In the reaction medium, DMF reduces Ag$^+$ into Ag nanoparticles[20,38,39] and PVF$_2$ present in the medium helps to stabilize the Ag nanoparticles. The formation of Ag nanoparticles is accompanied by color changes with time from colorless to pale yellow to reddish brown and finally to deep reddish brown, violet, or gray, depending on the concentration of AgNO$_3$ in the reaction medium. Thus the color change of the reaction mixture is a time-dependent process. In Figure 1, the optical characterization of the reaction mixture is presented for different aging times. In each figure at about 42 h of aging there is an absorption peak at the wavelength range 413–420 nm. With more aging, the intensity of the peaks gradually increased and also the peak showed a red shift to a maximum wavelength of 534–582 nm on the 13th day of aging depending on the AgNO$_3$ concentration in each set of the experiment. The origin of the UV–vis peak is due to the formation of a surface plasmon band of metallic silver.[7,40] This increase in the intensity may be attributed to the increasing concentration of silver nanoparticles produced from the reduction of AgNO$_3$ by DMF, and the red shift of the plasmon band is due to the increasing size of the Ag nanoparticles in the reaction medium.[16,18,20,23,41,42] The red shift of the plasmon band also depends on the shape, interparticle interaction, and dielectric constant of the medium.[18,22,23] In our experiment, the nanoparticles are grown in PVF$_2$ solution and therefore the dielectric constant remains almost the same during the experiment. Also, since the solution is very dilute with respect to silver concentration, the effect of interparticle interaction is also negligible. In the following treatment, we shall shed light on the size and shape of the nanoparticle nuclei. As the final shape of the nanoparticle arises from the shape of the nuclei so the growth of the nuclei with aging time may be approximated as independent of shape. The full width at the half-maximum (fwhm) of the absorption peaks gradually increases with time in each set of experiment. This indicates that with increasing aging time polydispersity of the nanoparticles increases. In Set-3, one important observation is that the 306-h absorption peak decreases in intensity than that of 232 h, but this is not observed for the lower AgNO$_3$ content samples (Set-1 and Set-2). Probably at the higher concentration of silver nanoparticles at this set, they produce clusters decreasing the nanoparticle concentration causing a decrease in the plasmon band intensity. During this period, the plasmon peak position shifts from 520 to 580 nm, supporting the increasing size of the nanoparticles. The peak is also flattened, suggesting a wide distribution of the nanosized particles at this state. Thus it may be surmised from these results that stable silver nanoparticles can be prepared with PVF$_2$ as stabilizer from the dilute AgNO$_3$ solution ($\leq 7.36 \times 10^{-3}$ M) using DMF as a reducing agent.

An analysis of time-dependent spectroscopic data may be done to get an insight of the nucleation and growth mechanism of silver nanoparticles. In Figure 2a–c, the absorbance at the
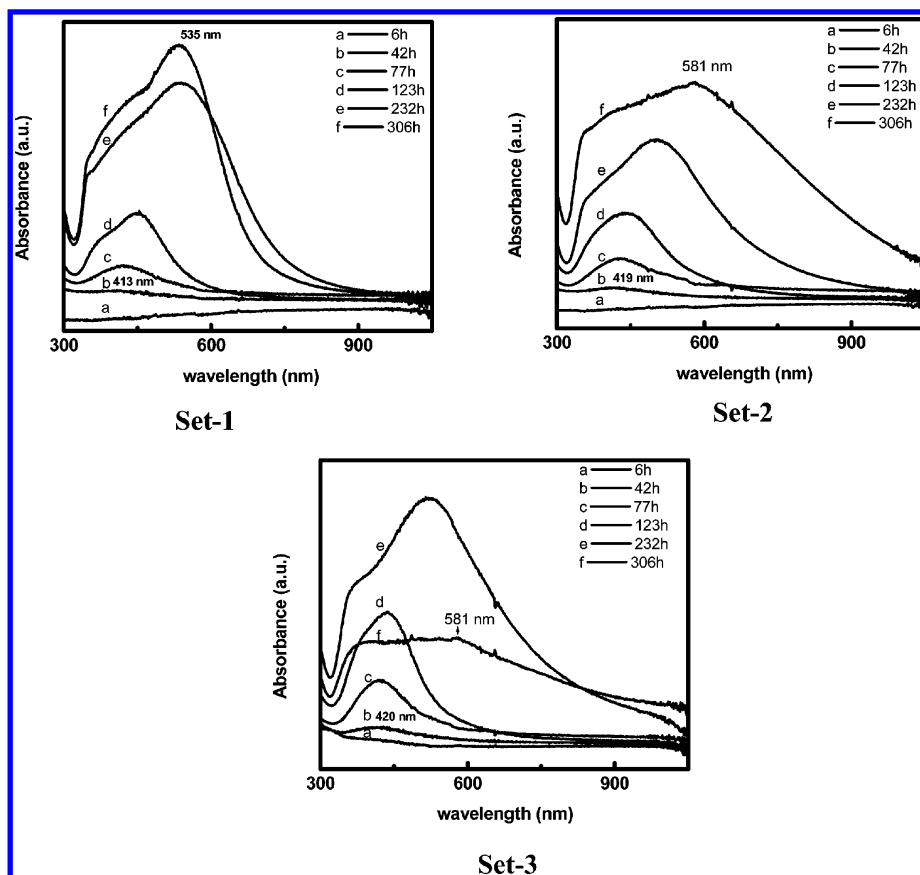
Figure 1. UV−vis absorption spectra of the reaction mixtures at different aging times. (a) Set-1 (PNC0.5). (b) Set-2 (PNC2.5). (c) Set-3 (PNC11).
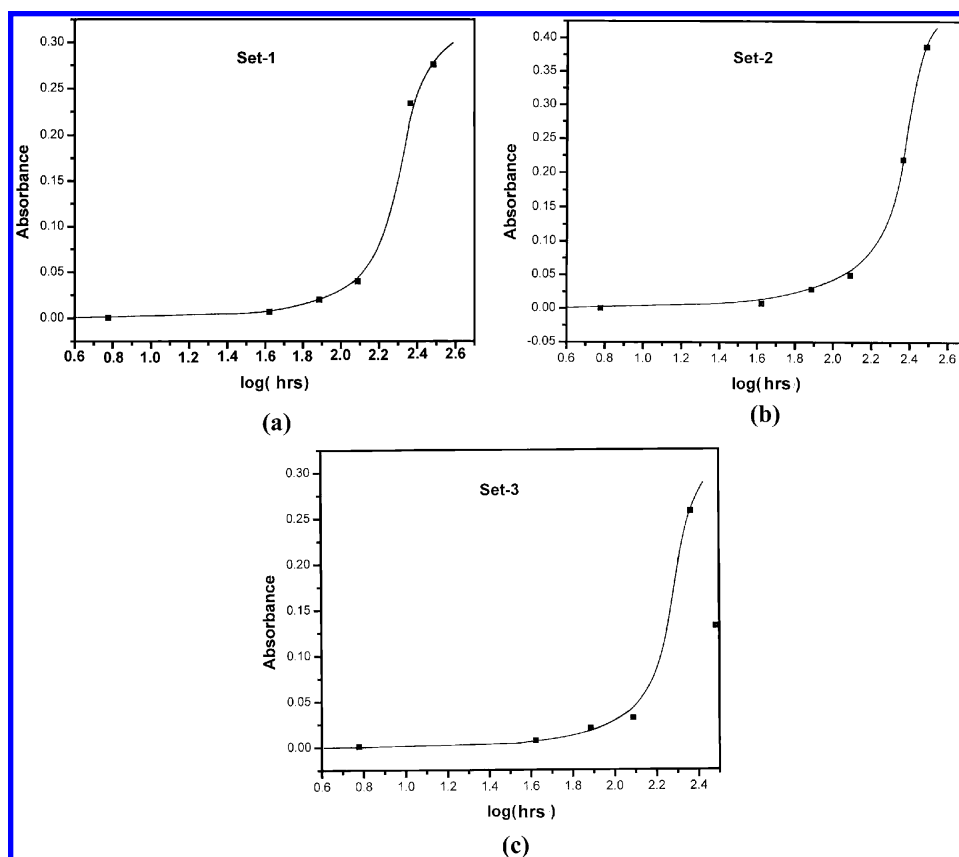
Figure 2. Absorbance of the plasmon band vs log[time (h)] plot for the indicated sets of reaction mixture at their highest peak position (306 h).

highest peak position is plotted with log(time) for the three sets of data. A sigmoidal rise of absorbance with time is evident in each plot. This is very similar to the crystallization isotherms of polymers, indicating the nucleation and growth of nano-particle as an autocatalytic process.[43] At longer time a saturation is observed in the Set-1 data, Set-2 data almost reaches a
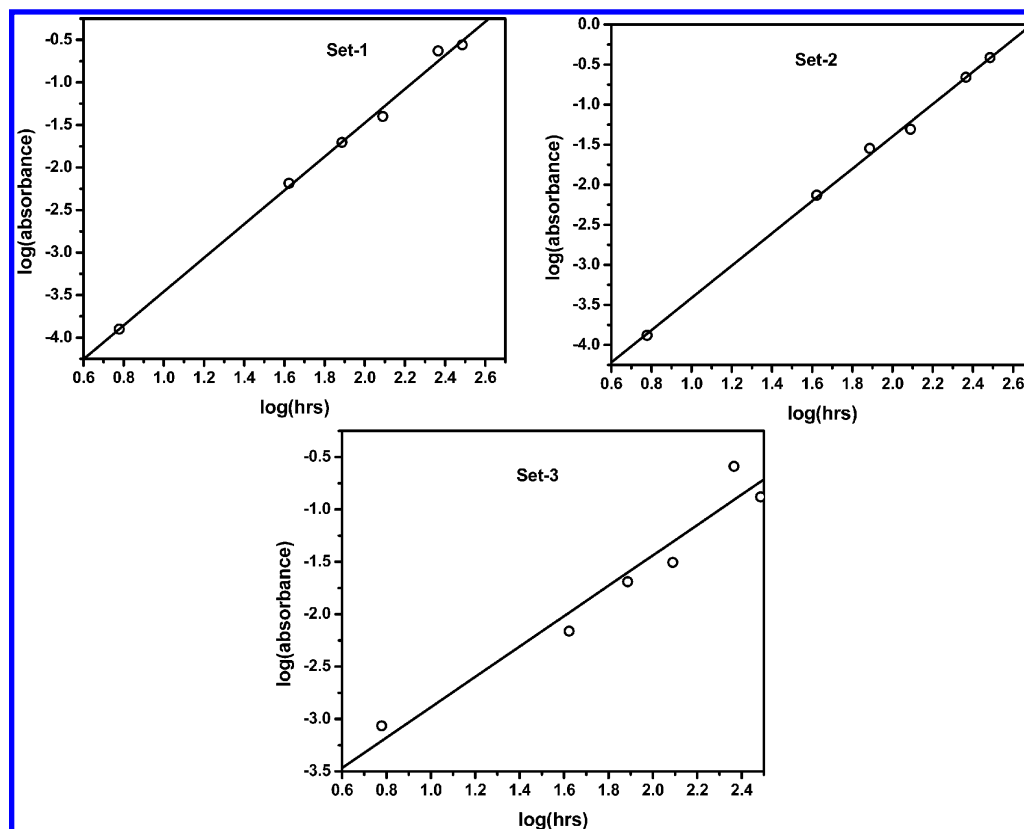
Figure 3. Avrami plot for the nanoparticle growth in the indicated sets of reaction mixture.

TABLE 1: Avrami Exponent "*n*" and Rate Constant "*k*" of Nanoparticle Formation in the PNCs Measured from UV−Vis Study

sample	slope "*n*"	intercept log(k)	correlation coefficient
PNC0.5	1.98	−5.44	0.998
PNC2.5	2.02	−5.43	0.998
PNC11	1.45	−4.34	0.973

saturation value, but Set-3 shows a decrease probably due to the impingement of the nanoparticles causing cluster formation.

The growth of a new phase in the mother phase is usually explained from the Avrami equation:[43,44]

$$1 - \lambda(t) = 1 - \exp(-kt^n) \qquad (1)$$

where $1 - \lambda(t)$ is the fraction transformed, "k" is the rate constant, "t" is the time of transformation, and "n" is a constant whose value depends on the nature of nucleation and growth process. On expanding, disregarding the higher terms and taking logarithm eq 1 transforms into

$$\log[1 - \lambda(t)] = \log k + n \log t \qquad (2)$$

Thus, a plot of log[1 − $\lambda(t)$] against log(t) would yield a straight line at the low conversion, and from the slope and intercept the "n" and "k" values can be calculated. As the absorbance at a particular wavelength depends on the nanoparticle concentration, so log[1 − $\lambda(t)$] may be approximated as log[absorbance]. In Figure 3, log[absorbance] versus log(t) plots are presented for the highest peak position in each case. It is interesting that, disregarding the saturation data, all the data fit in a straight line in each set. The slope, intercept, and correlation coefficient values are presented in Table 1. As apparent from the table, the rate constant "k" values of the process are almost the same for Set-1 and Set-2, while for Set-3 the values are somewhat higher. The Avrami exponent value is close to 2 for Set-1 and
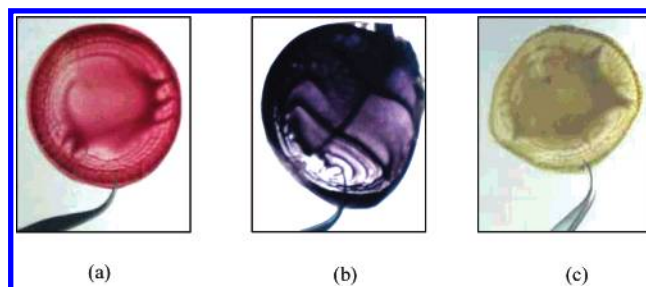

Figure 4. Normal (colored) pictures of Ag−PVF$_2$ nanocomposite films showing different colors. (a) PNC0.5. (b) PNC2.5. (c) PNC11 (pure PVF$_2$ film is almost transparent).

Set-2; however, it is close to 1.5 for Set-3. These exponent values are best explained with two-dimensional homogeneous nucleation with linear or diffusion-controlled growth.[43,44] In the case of Set-3, the lower "n" value certainly indicates a diffusion-controlled growth due to the higher concentration of the nuclei of nanoparticles as compared to those of the other sets.

Morphological Investigation. In Figure 4, the normal pictures of dried films prepared from 13-day-old solutions are presented. The three films have three different colors: Set-1 is reddish brown, Set-2 is violet, and Set-3 film is gray. The color is similar to the respective solutions from which these are prepared. This indicates that the nanoparticle dimensions do not change during the drying process. The TEM micrographs of the grids prepared from 13-day-old AgNO$_3$−PVF$_2$ solutions are presented in Figure 5 for the three sets of experiments. There are both rodlike and spherical morphologies of the nanoparticles in each set. The dimension of the Ag nanoparticles varies from 15 to 150 nm in the different sets of experiment. In Set-1 and Set-2, there is a proportion of rodlike morphology larger than that of Set-3 where some agglomerated nanoparticles are also observed. Probably due to the higher concentration of AgNO$_3$ in this set than those of the others, the nucleation density is
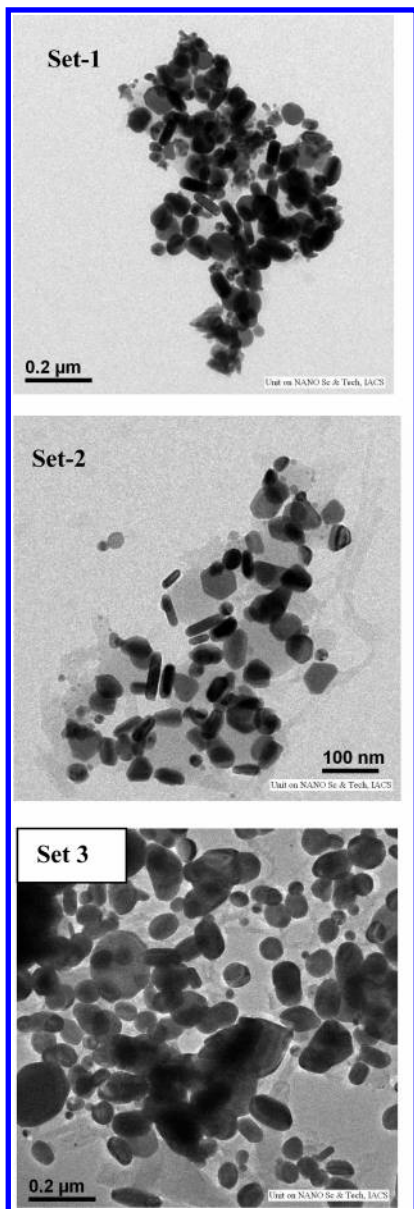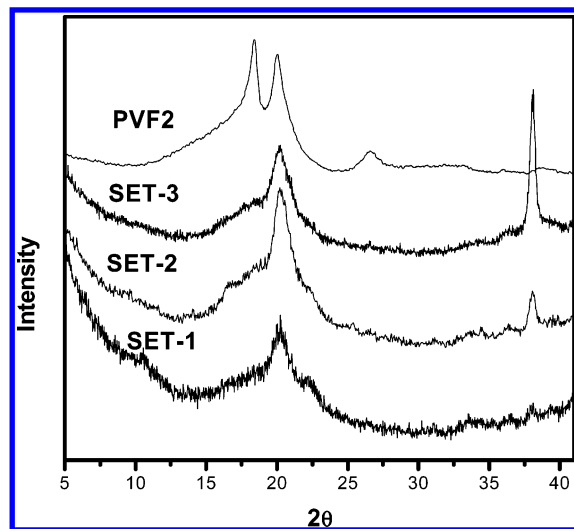
Figure 5. TEM pictures of Ag−PVF$_2$ nanocomposites. (a) Set-1 (PNC0.5). (b) Set-2 (PNC2.5). (c) Set-3 (PNC11).

Figure 6. WAXS patterns of PVF$_2$ and the nanocomposite films. Set-1 (PNC0.5). Set-2 (PNC2.5). Set-3 (PNC11).

larger and this causes cluster formation. Such an explanation is also supported from the Set-3 UV−vis data where the absorbance value decreases with the longest aging time. The polymer has a contrast much lower than that of metallic silver and is not distinctly observed in any of the TEM pictures.

Both TEM and UV−vis spectra indicate that the distribution of silver nanoparticle size is broad in the composites. No definite reason is known, and it may be attributed to the very slow reaction rate (e.g., 13 days to complete) used for preparing the nanoparticles. Another cause may be the absence of any surfactant or template in the preparation of nanoparticles. From the electron micrographs, it may be noted that the nanoparticles are of different shapes (spheroidal and rodlike) and the crystalline facets are not sharp. This indicates that there is no preferential attachment of PVF$_2$ on the nanoparticle facets.[45,46] The PVF$_2$ serves only as a stabilizer preventing aggregation of silver nanoparticles.

WAXS Study. The X-ray diffractograms of the PVF$_2$−Ag nanocomposite are compared in Figure 6. It is clear from the figure that there is a major difference in the X-ray patterns between pure PVF$_2$ and those of the nanocomposites. The diffractograms of pure PVF$_2$ have peaks at $2\theta = 18.4°$ and 20°, which correspond to those of α-polymorph. But the diffractograms of the composites have only a sharp peak at $2\theta = 20°$ that characterizes β-polymorph[47,48] of PVF$_2$. A diffraction peak around $2\theta = 38°$ is observed in the diffractograms of each nanocomposite for silver, and it gradually grew in size from Set-1 to Set-3. This is due to the increasing concentration of silver nanoparticles in the composites. It is really an interesting observation that Ag nanoparticles induce PVF$_2$ to crystallize in zigzag β-conformation. It may be probable that the interaction of the >CF$_2$ dipole of PVF$_2$ with Ag nanoparticle induces the −CH$_2$−CF$_2$− unit to adopt an all-trans conformation rather than the usual *TGTḠ* conformation. Priya and Jog also obtained a similar β-polymorphic PVF$_2$ in the PVF$_2$−bentonite clay nanocomposite.[6]

FTIR Study. In Figure 7, the FTIR spectra of PVF$_2$ and those of the nanocomposites are compared. It is apparent from the figure that the spectra of the nanocomposites are different from that of the pure PVF$_2$, which shows infrared absorption characteristics of a α-polymorph PVF$_2$ (796, 615, and 529 cm^{-1}).[49,50] On the other hand, the nanocomposite spectra show the characteristics of β-polymorph PVF$_2$ having peaks at 510 and 483 cm^{-1}.[49−51] Thus, the silver nanoparticles induce PVF$_2$ to crystallize in β-polymorph, supporting the X-ray observation. The different peak positions of PVF$_2$ in the nanocomposite and of the solvent cast PVF$_2$ are presented in Table 2. It is apparent from the table and also from Figure 7 that apart from the characteristic α-polymorph peaks the peaks at 976 and 764 cm^{-1} are also absent in the nanocomposite spectra. The 764 cm^{-1} peak is for the CF$_2$ bending and for the skeletal CF−CH−CF bending.[37] Probably an electrostatic interaction between the CF$_2$ dipole and the absorbed charges on the Ag nanoparticle causes the above vibrational motions to be ceased. Also, due to the attachment of heavier Ag atoms on the CF$_2$ dipole for the above interaction the CH$_2$ twisting vibration (976 cm^{-1}) is also ceased. Due to this electrostatic interaction of the nanoparticle with the >CF$_2$ dipole, the PVF$_2$ chain becomes straightened, forming the zigzag conformation of β-polymorph instead of the coiled *TGTG* conformation. The absence of the α-polymorph and formation of only β-polymorph in the composites may be explained from the nucleation of PVF$_2$ on the nanoparticle surface. PVF$_2$ is adsorbed on the nanoparticle surface in the all-trans conformation due to interaction of Ag nanoparticles with the >CF$_2$ dipole. The nuclei then grew to produce the

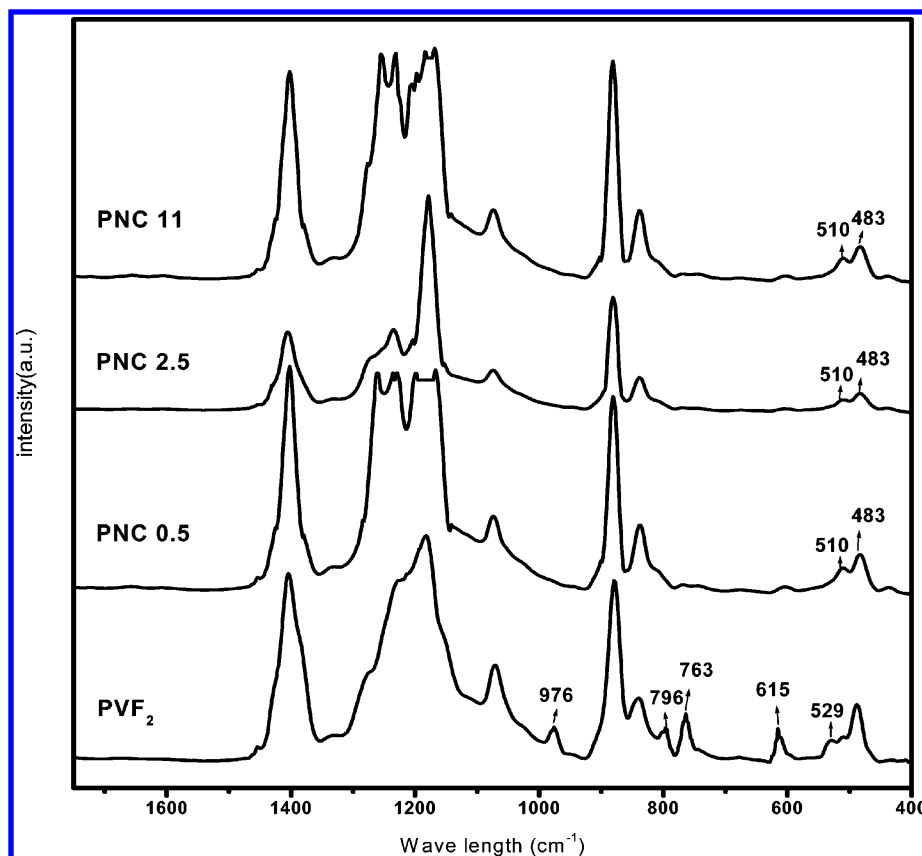**Figure 7.** FTIR spectra of PVF$_2$ and the nanocomposite films at indicated concentrations.

**TABLE 2: FTIR Peak Positions (cm^{-1}) of PVF$_2$ and Its Composites with Ag Nanoparticles**

PVF$_2$ solvent cast	PNC0.5	PNC2.5	PNC11
3024	3022	3021	3021
2983	2980	2979	2979
1404	1402	1405	1402
	1260		1254
	1236	1234	1231
			1205
			1197
1182	1198	1178	1183
	1167		1168
1071	1074	1074	1074
976			
879	881	881	881
839	838	838	838
796			
764			
615	603	603	603
529			
509	510	510	510
488	483	483	483
	437	439	439

piezoelectric β-polymorphic crystal of PVF$_2$. Since all the PVF$_2$ chains crystallize in β-polymorph, it may be argued that the nanoparticle nucleated crystallization of PVF$_2$ is of lesser nucleation energy than that of non-nanoparticle nucleated α-nuclei.

Thermal Study. The DSC thermograms of PVF$_2$ and its nanocomposites are presented in Figure 8a,b for the heating and cooling processes. It is a very interesting observation that the melting temperatures of PVF$_2$ nanocomposites are increased compared to that of pure PVF$_2$ (Figure 8a). The Ag nanoparticles influence the PVF$_2$ to crystallize in β-form, which has a higher melting point than that of the *TGTḠ* conformer (α-form). The melting points are 173.0, 175.5, 174.4, and 174.2 °C for the

pure PVF$_2$, PNC0.5, PNC2.5, and PNC11 nanocomposites, respectively. Thus, with inclusion of Ag nanoparticles at low nanoparticle concentration, the melting point has increased, but with increasing nanoparticle concentration the melting point then decreased, though it is greater than that of pure PVF$_2$. Such a decrease in the melting points of β-phase PVF$_2$ with increasing nanoparticle concentration might arise for different reasons, such as the interaction of nanoparticles with PVF$_2$ or with increasing size of nanoparticles. It appears from our earlier results that both the factors may be responsible for this apparent decrease of melting point. The enthalpy of fusion values of PVF$_2$ are 53, 58, 56, and 53 J/g in pure PVF$_2$, PNC0.5, PNC2.5, and PNC11 nanocomposites, respectively. The results show variation similar to that of the melting point data with composition, and the higher enthalpy of fusion values of PNC0.5 and PNC2.5 nanocomposites might be attributed to the better packing of the zigzag β-PVF$_2$ chain than that of the *TGTḠ* α-chain. With increase in size of nanoparticles in PNC11, the packing of β-PVF$_2$ is less perfect, causing decrease of enthalpy of fusion and melting point. In Figure 8b, the crystallization isotherms of PVF$_2$ and nanocomposites are compared for crystallization from the melt at the cooling rate of 5 °C/min. The peak temperatures of the exotherms are 142.5, 148.8, 145.7, and 145.6 °C for PVF$_2$, PNC0.5, PNC2.5, and PNC11, respectively. Thus, the PNCs have crystallization temperatures higher than that of pure PVF$_2$, indicating that the Ag nanoparticles act as nucleating agents of PVF$_2$ crystallization in the composite. However, with increasing nanoparticle concentration, the nucleating effect decreases. The reason is not yet known to us.

In Figure 9, the TGA thermograms of pure PVF$_2$ and its nanocomposites are compared. It is apparent from the figure that PVF$_2$ exhibits two-step degradation: the first one occurs at 476 °C, and the second one occurs at 554 °C. During the degradation process, it evolves hydrogen fluoride along with a
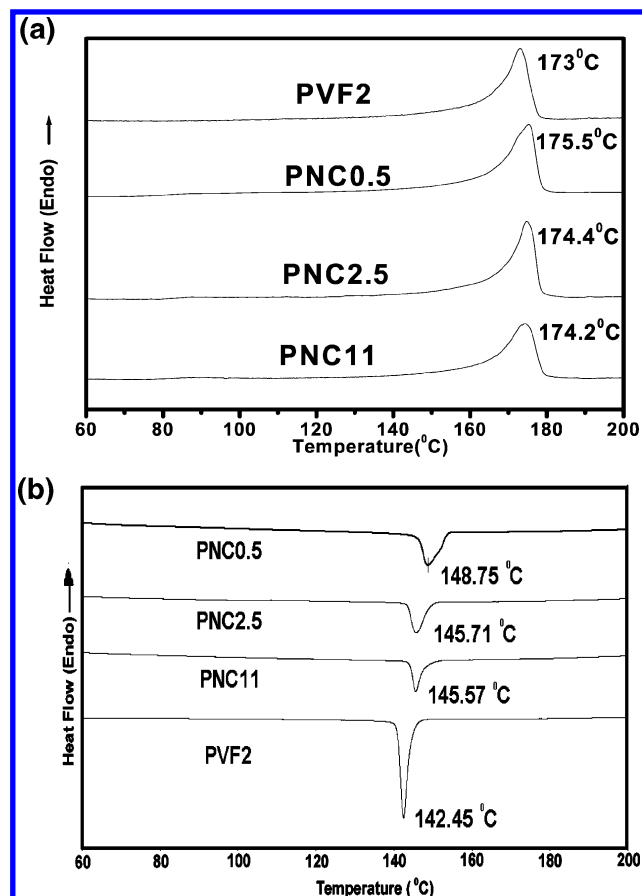
Figure 8. (a) DSC melting endotherms of PVF_2 and the nanocomposites at indicated compositions. (b) Crystallization isotherms of PVF_2 and the PNCs at indicated compositions for cooling from the melt at the rate of 5° C/min.
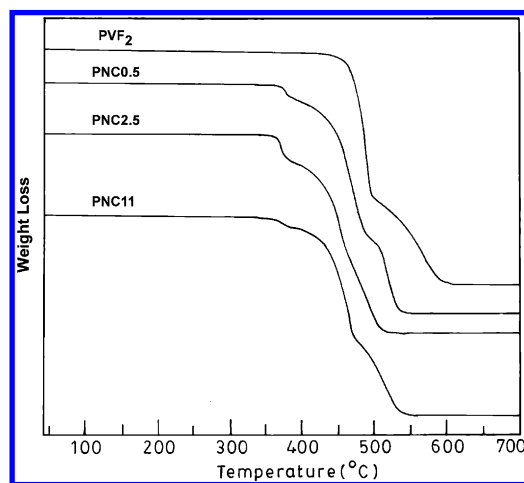
Figure 9. TGA thermograms of PVF_2 and the nanocomposite films at indicated compositions. The ordinate scale has been shifted for clarity.

monomer and a small amount of $C_4H_3F_3$.[52] Similar two-step degradation of PVF_2 was also observed by other groups.[53] In the nanocomposites, as evident from the figure, degradation in each case is a three-step process. Here the new inflection in TGA thermograms occurs at much lower temperature (e.g., 369 °C), and the percentage weight loss at this new step is different in different nanocomposites. For example, the PNC0.5 exhibits a 7% weight loss at this step while PNC2.5 exhibits a 14% weight loss. This increased weight loss may be attributed to the higher nanoparticle concentration. The size of nanoparticles might also have some influence on the degradation, and this is

TABLE 3: Inflection Points of TGA Thermograms of PVF_2 and Silver Nanocomposites[a]

samples	PVF_2 (new) (°C)	PVF_2 (1) (°C)	PVF_2 (2) (°C)	residual wt % (w/w)
PVF_2		476	554	0
PNC0.5	369	455	509	0.77
PNC2.5	369	444	487	1.73
PNC11	362	454	510	4.46

[a] Numbers in parenthesis indicate the stage of degradation.

apparent from the TGA thermogram of PNC11 where the above weight loss is 4%. This is probably for the very large size of nanoparticles, which have a smaller surface area. Thus, it might be probable that the total surface area of the nanoparticles has some catalyzing effect in the degradation process. The polymer molecules attached to the nanoparticle surface degrade first, and this yields the new step of degradation process. After the degradation of the nanoparticle-attached material, it propagates in the two-step process as usual in PVF_2. But the degradation temperatures are much lower than those of PVF_2 (Table 3). It is apparent from the table that the $PVF_2(1)$ inflection point decreases by 21, 32, and 22 °C for PNC0.5, PNC2.5, and PNC11, respectively. Similarly the $PVF_2(2)$ inflection point decreases by 45, 67, and 44 °C, respectively, from that of PVF_2. The highest decrease in the $PVF_2(1)$ and $PVF_2(2)$ inflection point for PNC2.5 may be explained for the largest total surface area of Ag nanoparticles in nanocomposites due to the increased concentration of nanoparticles. The low decrease for PNC11 is due to the decrease of total surface area of nanoparticles for the agglomeration of nanoparticles arising from increased silver concentration. In a word, the nanoparticles enhance the degradation of their surrounding macromolecules by a mechanism that is not yet clear to us. The percentage of residual weights is also included in Table 3. It is evident from the data that there is an increase in the residual weight (w/w %) with increasing Ag concentration. This does not indicate that the thermal stability of nanocomposites has increased; rather, this increase in residual weight may be attributed to the increased Ag concentration, which is not completely decomposed during heating of the nanocomposite.

Mechanical Property. Figure 10a−c shows the temperature dependence of storage modulus, loss modulus, and tan δ of PVF_2 and three nanocomposites. The storage modulus (G′) relates the ability of the material to store or return energy when oscillatory force is applied to the specimen, and loss modulus (G″) relates the ability to lose the energy. From Figure 10a, it is apparent that in each case storage modulus decreases with increasing temperature, and above 150 °C it is negligibly small. The storage modulus of the nanocomposites is highest for the PNC 0.5 sample. It then decreases for the PNC 2.5 and PNC 11 samples, although the Ag nanoparticle concentration increases in these samples. The storage modulus of all the PNCs is higher than that of pure PVF_2, indicating mechanical reinforcement in the nanocomposites. In these thermograms, there is a break in the storage modulus temperature plot, and this is better represented in Figure 10b, where loss modulus values are plotted with temperature. Here the single break in the storage modulus− temperature plot is represented by one sharp peak and one small peak in each thermogram. The sharp peak may be considered as arising from the glass transition temperature (T_g) of PVF_2, and the T_g value increases in the PNC0.5 sample by 2.3 °C as compared to that of pure PVF_2. The T_g then decreases for the PNC2.5 and PNC11 samples, although its values are higher than that of pure PVF_2. However, the higher temperature peaks in loss modulus plots show a relatively higher increase in the PNCs
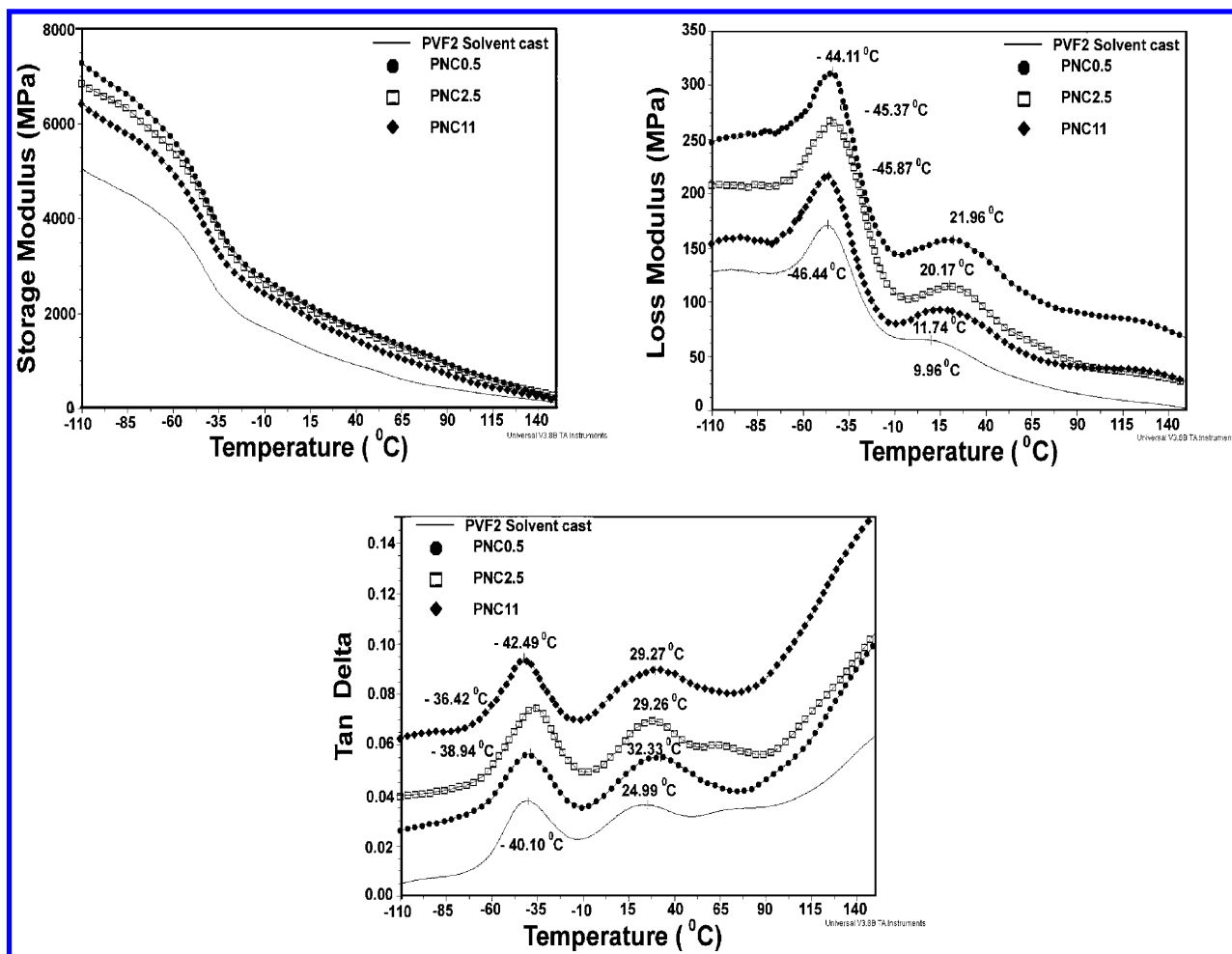
Figure 10. Mechanical property−temperature plots of PVF$_2$ and the PNCs. (a) Storage modulus. (b) Loss modulus. (c) tan δ.

TABLE 4: Summary of Mechanical Properties of PNCs Measured by DMA

| sample | $T_g{}^a$ (°C) | storage modulu s (MPa) | | | | | |
		−100 °C	% increase	−40 °C	% increase	20 °C	% increase
PVF$_2$ (solvent cast)	−46.4	4825		2742		1182	
PNC0.5	−44.1	7004	45	4271	55.8	2057	74
PNC2.5	−45.4	6658	38	4166	51.9	1972	66.8
PNC11	−45.9	6159	27.6	3688	34.5	1810	53.1

^{a} From the loss modulus plot (low-temperature peak).

(12° C for PNC0.5), but with an increase in the Ag concentration these peak temperatures also show similar decrease as in T_g. In Figure 10c, the tan δ versus temperature plot is compared for the pure PVF$_2$ and the nanocomposites. Here also two peaks are observed as in the loss modulus plot although the peak temperatures are 6−8° higher than those of the former. While the origin of the lower temperature peak may be the glass transition temperature at the amorphous zone, the origin of the higher temperature peak is yet unknown. Probably this peak is also similar to glass transition and the relaxation of the chain is occurring at the interface of the crystalline and amorphous region.[54]

The storage modulus values presented in Table 4 clearly indicate that there is significant mechanical property reinforcement in the PNCs. Due to the large surface area of Ag nanoparticles, such a large storage modulus enhancement (53−74%) occurred. It is also apparent that the mechanical property enhancement is the highest in PNC0.5 at all temperatures compared to that of the other PNCs. The PNC0.5 also has the highest melting point and enthalpy of fusion, that is, this

composite has better lattice packing than the others showing higher mechanical property. Also, at −100 °C, the increase of the storage modulus is lower (27−45%) than those of other temperatures for all the PNCs. This is because the reinforcement effect in the glassy state is lower than that in the rubbery state.[5] The larger increase of storage modulus values at higher temperature (Table 4) is due to the relatively free movement of the PVF$_2$ segments, and then the reinforcement effect of the Ag nanoparticle is more effective.

Conclusion

It may be concluded from this study that PVF$_2$ acts as a stabilizer of Ag nanoparticles produced in situ by the reduction of DMF. The dipolar interaction of the $>$CF$_2$ dipole with the surface charges of Ag nanoparticle stabilizes the nanoparticle, as evidenced from the FTIR spectra. The change of UV−vis spectra with time reflects a sigmoidal increase of absorbance with log(time), and analysis of these data indicate that the Avrami treatment may be applied to the growth analysis of the

nanoparticles in solution. The Avrami exponent has the value 2 for PNC0.5 and PNC2.5, while for PNC11 it is 1.5, signifying two-dimensional nucleation with linear or diffusion-controlled growth. The TEM micrographs indicate both spherical and rodlike morphology of Ag nanoparticles in the PNC0.5 and PNC2.5 samples. In PNC11, the morphology is mostly spherical with a tendency toward cluster formation. The melting temperature and enthalpy of fusion of PVF$_2$ have increased in small amount in the PNCs; however, with increasing Ag nanoparticle concentration they gradually decrease. The crystallization study on cooling from the melt indicates that silver nanoparticles act as a nucleating agent for crystallization of PVF$_2$. Contrary to the two-step degradation process in pure PVF$_2$, the PNCs exhibit a three-step degradation process and the degradation temperatures of PNCs are also lower than that of PVF$_2$. X-ray and FTIR study indicate that the β-polymorphic structure of PVF$_2$ is produced in the nanocomposite. The storage modulus data show a sharp increase in modulus values for the PNCs, although with increase in nanoparticle concentration the data decrease. Both loss modulus and tan δ curves exhibit two peaks: the lower one has been attributed to the glass transition of PVF$_2$ in the amorphous phase, and the higher one is due to the relaxation of the chain segments at the crystalline amorphous interface. The glass transition temperature shows a marginal increase in the PNCs, but the higher one shows somewhat of a higher increase.

References and Notes

(1) Giannelis, E. P.; Krishnamoorti, R.; Manias, E. *Adv. Polym. Sci.* **1999**, *138*, 107.

(2) Vaia, R. A.; Krishnamoorti, R. In *Polymer Nanocomposites: Synthesis, Characterization and Modeling*; Krishnamoorti, R., Vaia, R. A., Eds.; American Chemical Society: Washington, DC, 2001; p 1.

(3) Maiti, P.; Nam, P. H.; Okamoto, M.; Hasegawa, N.; Usuki, A. *Macromolecules* **2002**, *35*, 2042.

(4) Alexandre, M.; Dubois, P. *Mater. Sci. Eng. Rev.* **2000**, *R28* (1−2), 1.

(5) Kuila, B. K.; Nandi, A. K. *Macromolecules* **2004**, *37*, 8577.

(6) Priya, L.; Jog, J. P. *J. Appl. Polym. Sci.* **2003**, *89*, 2036.

(7) Mbhele, Z. H.; Salemane, M. G.; van Sittert, C. G. C. E.; Nedeljkovic, J. M.; Djokovic, V.; Luyt, A. S. *Chem. Mater.* **2003**, *15*, 5019.

(8) Hussain, I.; Brust, M.; Papworth, A. J.; Cooper, A. I. *Langmuir* **2003**, *19*, 4831.

(9) Yu, S.-H.; Yoshimura, M.; Calderon Moreno, J. M.; Fujiwara, T.; Fujino, T.; Teranishi, R. *Langmuir* **2001**, *17*, 1700.

(10) Zhu, Y.; Qian, Y.; Li, X.; Zhang, M. *Chem. Commun.* **1997**, 1081.

(11) Dirix, Y.; Bastiaansen, C.; Caseri, W.; Smith, P. *J. Mater. Sci.* **1999**, *34*, 3859.

(12) Gaddy, G. A.; McLain, J. L.; Korchev, A. S.; Slaten, B. L.; Mills, G. *J. Phys. Chem. B* **2004**, *108*, 14858.

(13) Qian, X. F.; Yin, J.; Huang, J.-C.; Yang, Y. F.; Guo, X. X.; Zhu, Z. K. *Mater. Chem. Phys.* **2001**, *68*, 95.

(14) Malik, S.; Batabyal, S.; Basu, C.; Nandi, A. K. *J. Mater. Sci. Lett.* **2003**, *22*, 1113.

(15) Greenwood, N. N.; Earnshaw, A. *Chemistry of the Elements*, 2nd ed.; Butterworth-Heinemann: Oxford, 1997.

(16) Jin, R. C.; Cao, Y. W.; Mirkin, C. A.; Kelly, K. L.; Schatz, G. C.; Zheng, J. G. *Science* **2001**, *294*, 1901.

(17) Dickson, R. M.; Lyon, L. A. *J. Phys. Chem. B* **2000**, *104*, 6095.

(18) Kamat, P. V. *J. Phys. Chem. B* **2002**, *106*, 7729.

(19) Hongchao, J.; Charles Cao, Y.; Hao, E.; Metraux, S.; Schatz, G. C.; Mirkin, C. *Nature* **2003**, *425*, 487.

(20) Pastoriza-Santos, I.; Liz-Marzan, L. M. *Nano Lett.* **2002**, *2*, 903.

(21) Kreibig, U.; Volmer, M. *Optical Properties of Metal Clusters*; Springer-Verlag: Berlin, 1995.

(22) Mulvaney, P. *Langmuir* **1996**, *12*, 788.

(23) Liz-Marzan, L. M. *Langmuir* **2006**, *22*, 32.

(24) Michaels, A. M.; Nirmal, M.; Brus, L. E. *J. Am. Chem. Soc.* **1999**, *121*, 9932.

(25) Weiss, A.; Haran, G. *J. Phys. Chem. B* **2001**, *105*, 12348.

(26) Maier, S. A.; Kilk, P. G.; Atwater, H. A.; Meltzer, S.; Harel, E.; Koel, B. E.; Requicha, A. A. G. *Nat. Mater.* **2003**, *2*, 229.

(27) Zanchet, D.; Micheel, C. M.; Parak, W. J.; Gerion, D.; Williams, S. C.; Alivisatos, A. P. *J. Phys. Chem. B* **2002**, *106*, 11758.

(28) Jin, R.; Wu, G.; Li, Z.; Mirkin, C. A.; Schatz, G. C. *J. Am. Chem. Soc.* **2003**, *125*, 1643.

(29) Lovinger, A. J. In *Developments in crystalline polymers-1*; Bassett, D. C., Ed.; Applied Science Publishers: London, 1981; p 195.

(30) Doll, W. W.; Lando, J. B. *J. Macromol. Sci., Phys. B* **1970**, *4*, 309.

(31) Hasegawa, R.; Takahashi, Y.; Chatani, Y.; Tadokaro, H. *Polym. J.* **1972**, *3*, 600.

(32) Wang, T. T.; Herbert, J. M.; Glass, A. M. In *The Applications of Ferroelectric Polymers*; Blackie & Sons Ltd.: London, 1988.

(33) Lando, J. B.; Olf, H. G.; Peterlin, A. *J. Polym. Sci.* **1966**, *4*, 941.

(34) Weinhold, S.; Litt, M.; Lando, J. B. *J. Polym. Sci.* **1979**, *17*, 585.

(35) Nandi, A. K.; Mandelkern, L. *J. Polym. Sci., Part B: Polym. Phys.* **1991**, *29*, 1287.

(36) Roerdink, E.; Challa, G. *Polymer* **1980**, *21*, 509.

(37) Belke, R. E.; Cabasso, I. *Polymer* **1988**, *29*, 1831.

(38) Pastoriza-Santos, I.; Liz-Marzan, L. M. *Pure Appl. Chem.* **2000**, *72*, 83.

(39) Pastoriza-Santos, I.; Liz-Marzan, L. M. *Langmuir* **2002**, *18*, 2888.

(40) Sun, Y.; Yin, Y.; Mayers, B. T.; Herricks, T.; Xia, Y. *Chem. Mater.* **2002**, *14*, 4736.

(41) Henglein, A.; Meisel, D. *Langmuir* **1998**, *14*, 1392.

(42) Link, S.; El-Sayed, M. A. *J. Phys. Chem. B* **1999**, *103*, 4212.

(43) Mandelkern, L. *Crystallization of Polymers*, 2nd ed.; Cambridge University Press: New York, 2004; Vol. 2, p 1.

(44) Wunderlich, B. *Macromolecular Physics*; Academic Press: New York, 1976; Vol. 2, p 115.

(45) (a) Wiley, B.; Sun, Y.; Chen, J.; Cang, H.; Li, Z.-Y.; Li, X.; Xia, Y. *MRS Bull.* **2005**, *30*, 356. (b) Im, S. H.; Lee, Y. T.; Wiley, B.; Xia, Y. *Angew. Chem., Int. Ed.* **2005**, *44*, 2154.

(46) Gao, Y.; Jiang, P.; Song, L.; Liu, L.; Yan, X.; Zhou, Z.; Liu, D.; Wang, J.; Yuan, H.; Zhang, Z.; Zhao, X.; Dou, X.; Zhou, W.; Wang, G.; Xie, S. *J. Phys. D: Appl. Phys.* **2005**, *38*, 1061.

(47) Lando, J. B.; Doll, W. W. *J. Macromol. Sci., Phys.* **1968**, *B2*, 205.

(48) Guerra, G.; Karasz, F. E.; MacKnight, W. J. *Macromolecules* **1986**, *19*, 1935.

(49) Enomoto, S.; Kawai, Y.; Sugita, M. *J. Polym. Sci., Part A-2* **1968**, *6*, 861.

(50) Tashiro, K.; Kobayashi, M. *Phase Transitions* **1989**, *18*, 213.

(51) Cortili, G.; Zerbi, G. *Spectrochim. Acta, Part A* **1967**, *23*, 2216.

(52) Zulfiqar, S.; Zulfiqar, M.; Rizvi, M.; Munir, A.; McNeill, IC. *Polym. Degrad. Stab.* **1994**, *43*, 423.

(53) Malmonge, L. F.; Mattoso, L. H. C. *Polymer* **2000**, *41*, 8387.

(54) Liu, Z.; Marechal, P.; Jerome, R. *Polymer* **1997**, *38*, 4925.